FULL PAPER

Perfect Vortex

ADVANCED
OPTICAL
MATERIALS

www.advopticalmat.de

Generating Focused 3D Perfect Vortex Beams By Plasmonic Metasurfaces

Yuchao Zhang, Weiwei Liu, Jie Gao,* and Xiaodong Yang*

Perfect vortex (PV) beams possessing annular intensity profiles independent of topological charges promise significant advances in particle manipulation, fiber communication, and quantum optics. The PV beam is typically generated from the Fourier transformation of the Bessel–Gauss beam. However, the conventional method to produce PV beams requires a series of bulky optical components, which greatly increases the system complexity and also hinders the photonic device integration. Here, plasmonic metasurfaces made of rectangular-hole nanoantennas as integrated beam converters are designed and demonstrated to generate focused 3D PV beams in a broad wavelength range, by combining the phase profiles of axicon, spiral phase plate, and Fourier transform lens simultaneously based on the Pancharatnam–Berry phase. It is demonstrated that the PV beam structures can be adjusted by varying several control parameters in the metasurface design. Moreover, multiple PV beams with arbitrary arrangement and topological charges are also produced. These results have the promising potential for enabling new types of compact optical devices for tailoring complex light beams and advancing metasurface-based functional integrated photonic chips.

1. Introduction

Optical vortex beams with helical wavefront carrying orbital angular momentum (OAM) have drawn considerable attention in many exciting fields such as quantum information processing,[1–3] optical trapping,[4,5] and optical communications.[6,7] Since the ring radius of vortex intensity profile strongly depends on the topological charge (TC), it is not easy to couple multiple OAM beams simultaneously into single air-core fiber used for multiplexed communications.[8–10] In order to solve the above issue, perfect vortex (PV) beams have been proposed to possess unchanged annular intensity profiles independent of TCs.[11–19] The PV beams have the same vortex ring radius and beam divergence for different TCs, enabling their special applications in particle manipulation,[20] plasmonic enhancement,[21] optical communication,[22,23] quantum optics,[24] and laser manufacturing.[25] The PV beam is typically produced

Dr. Y. Zhang, Dr. W. Liu, Prof. J. Gao, Prof. X. Yang
Department of Mechanical and Aerospace Engineering
Missouri University of Science and Technology
Rolla, MO 65409, USA
E-mail: gaojie@mst.edu; yangxia@mst.edu

from the Fourier transformation of the Bessel–Gauss (BG) beam,[13,14] by utilizing a series of free-space bulky optical components including axicon, spiral phase plate, Fourier transform lens, and spatial light modulator. This fact greatly increases the optical system complexity and also hinders the device integration in OAM-based photonic circuits.

Recently, plasmonic metasurfaces made of subwavelength nanoantenna arrays in thin metallic films have provided a powerful and efficient platform for manipulating the intensity, wavefront, and polarization of light beams beyond the diffraction limit.[26,27] In contrast to the bulky optical components with wavelength-dependent phase shift based on optical path difference, in the Pancharatnam–Berry phase optical elements (PBOEs), the PB phase in broadband operation originating from the geometric phase and accompanied polarization conversion is introduced.[28–34] The PBOE-based metasurfaces have been widely designed for wavefront shaping applications in making on-chip structured beam generators,[35–45] flat lenses,[46–49] ultrathin wave plates,[50–52] and holograms.[53–57]

In this work, we present PBOE-based plasmonic metasurfaces made of rectangular-hole nanoantenna arrays as integrated optical beam converters for the direct generation of the focused 3D PV beams, without using bulky optical components, such as axicon, lens, and spatial light modulator. The PB phase profiles encoded on metasurfaces are uniquely designed with the combined phase distributions of axicon, spiral phase plate, and Fourier transform lens. The single ultrathin plasmonic metasurface device with compact area of 50 μm × 50 μm can create 3D PV beam in a long propagation distance and operate in a broad wavelength range from 600 to 1000 nm, which is useful in wavelength-multiplexed OAM-based optical fiber communication. For comparison, the previously demonstrated PB phase element system used to produce PV beams contains three in-sequence metasurface plates with efficient diameters ≥6 mm fabricated in glass boards, with the single operating wavelength at 632.8 nm.[13] It is shown that the obtained PV beams have the almost constant vortex ring radius and the same beam divergence for different TCs. We also demonstrate that the PV beam structures can be easily adjusted by varying several control parameters in the metasurface design including axicon period, lens focal length, and operation wavelength. Furthermore, multiple PV beams with

**ADVANCED
SCIENCE NEWS**
www.advancedsciencenews.com

**ADVANCED
OPTICAL
MATERIALS**
www.advopticalmat.de

arbitrary location arrangement and different TCs have also been produced by superimposing the complex amplitudes of several single PV beams propagating along different diffraction angles. Our demonstrated results will enable new types of ultra-compact optical devices for manipulating complex structured beams, and also advance metasurface-based functional integrated photonic chips.

2. Results and Discussion

As shown in **Figure 1**a, the plasmonic rectangular-hole nano-antenna etched in a thin gold film on glass substrate is used for the construction of PBOE-based anisotropic and inhomogeneous metasurfaces. The period of the unit cell is 330 nm, the width and length of the rectangular hole is 60 and 200 nm respectively, and the thickness of the gold film is 50 nm. The rotation angle of the rectangular-hole antenna is defined by θ. According to the PBOE principle, when the incident circularly polarized beam normally transmits through the anisotropic rectangular-hole antenna, the transmitted beam will contain both the original spin component with no phase shift and the converted spin component with the induced PB phase shift of 2θ. The desired phase profile is then obtained by arranging the anisotropic rectangular-hole antennas with specified rotation angles into a designed spatially inhomogeneous array. Figure 1b gives the simulated transmission phase shifts for the transmitted converted spin component from the rectangular-hole antennas in different rotation angles. It can be seen that in the broad wavelength range from 600 to 1000 nm, the phase shift variations of the converted spin component for the rectangular-hole antennas are twice as their rotation angles, which verifies the broadband PB phase modulation with the rectangular-hole antennas.

The simulated optical field $|E|$ distributions of rectangular-hole antennas under orthogonal polarizations with both linear polarization basis (vertical and horizontal linear polarizations, VLP and HLP) and circular polarization basis (left-handed and right-handed circular polarizations, LCP and RCP) at 800 nm is shown in Figure 1c, where strong polarization anisotropy is observed. Figure 1d shows the fabricated homogeneous array of rectangular-hole antennas etched by a focus ion beam (FIB) system in a 50 nm thick-gold film on glass substrate with the metasurface area of 50 μm × 50 μm. Next, the transmission spectra are measured and simulated under both linear and circular polarization basis. As plotted in Figure 1e, the transmission spectra through rectangular-hole antennas under VLP and HLP indicate a strong anisotropy in a broad wavelength
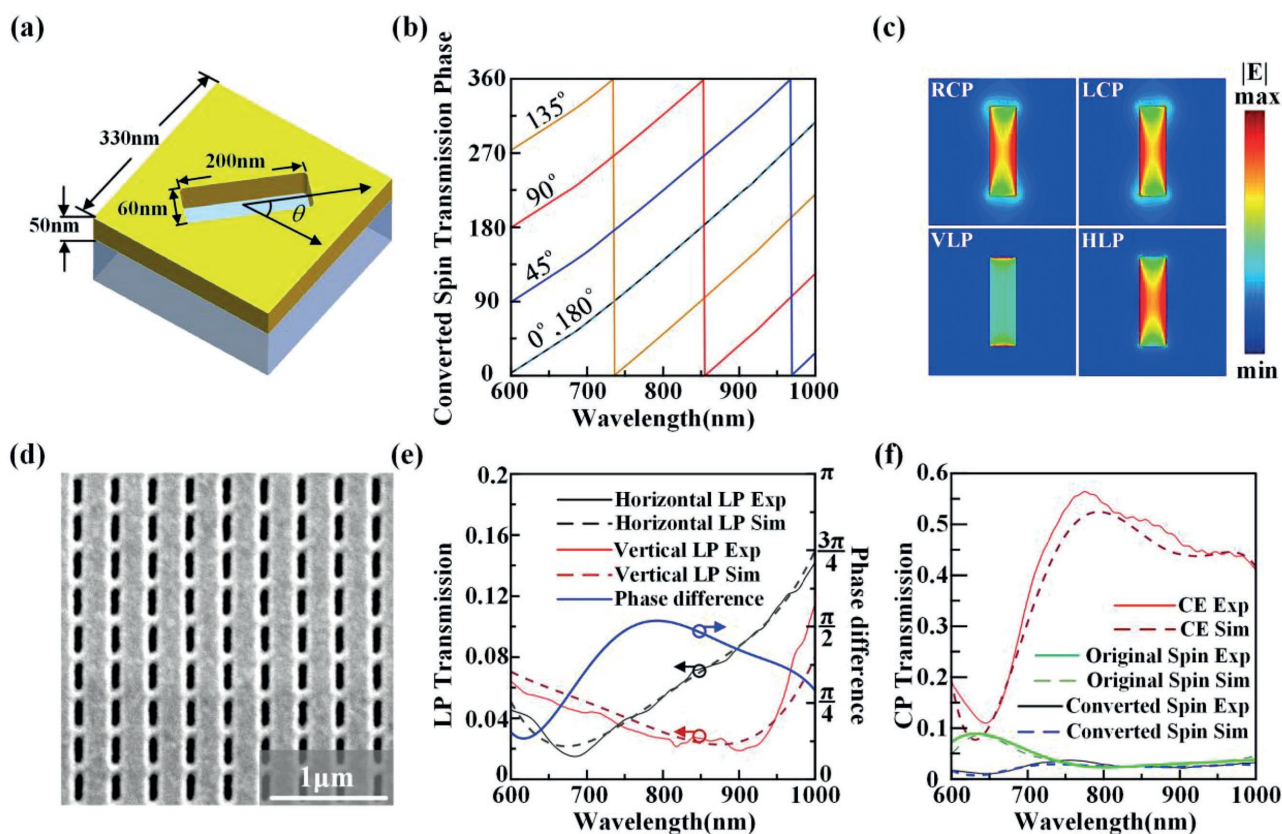
Figure 1. a) Schematic of the unit cell design of the rectangular-hole antenna at rotation angle of θ. b) The transmission phase shift spectra of the unit cell for the converted spin component at rotation angles of 0, 45°, 90°, 135°, and 180°. c) Simulated optical field $|E|$ distributions of rectangular-hole antennas under orthogonal polarizations at 800 nm. d) A SEM image of the fabricated rectangular-hole antenna array. e) Measured and simulated transmission spectra under linear polarization basis, and the phase difference between HLP and VLP. f) Measured and simulated transmission spectra and conversion efficiency spectra under circular polarization basis.

ADVANCED
SCIENCE NEWS
www.advancedsciencenews.com

ADVANCED
OPTICAL
MATERIALS
www.advopticalmat.de

range. Besides, the simulated phase difference between HLP and VLP plotted in Figure 1e is around $\pi/2$ near 800 nm, indicating that the current PBOE design is close to a quarter-wave plate and thus the polarization converted efficiency is around 50%, as shown in Figure 1f. For the transmission under circular polarization basis, the incident beam has LCP and the total transmitted beam through the metasurface contains both the LCP (original spin) component and the RCP (converted spin) component. The original spin transmission is defined as the intensity ratio between the transmitted LCP component and the incident LCP beam, while the converted spin transmission is defined as the intensity ratio between the converted RCP component and the incident LCP beam. The polarization conversion efficiency is defined as the intensity ratio between the converted spin component and the total transmitted beam. Figure 1f plots the measured and simulated spectra of original spin transmission (LCP, green line), converted spin transmission (RCP, blue line), and conversion efficiency (CE, red line). The observed maximum CE is around 55% near 800 nm, where the plasmonic resonance occurs.

By rotating the rectangular-hole antenna inside the unit cell, the transmitted PB phase shift of the converted spin component can be obtained in broad bandwidth. The inhomogeneous rectangular-hole antenna arrays are then designed to form the PBOE-based plasmonic metasurfaces as integrated optical beam converters for the direct generation of the focused 3D PV beams in a broad wavelength range. The designed PB phase profile $\varphi_{PB}(x,y)$ encoded on the metasurface is a superposition of the phase distributions of axicon, spiral phase plate, and Fourier transform lens, as illustrated in **Figure 2**a. The rotation angle $\theta(x,y)$ of the rectangular-hole antenna in each unit cell is

then determined by $\theta(x,y) = \varphi_{PB}(x,y)/2$. The PB phase profile is defined by the following functions

$$\varphi_{PB}(x,y) = \varphi_{axicon}(x,y) + \varphi_{spiral}(x,y) + \varphi_{lens}(x,y) \tag{1}$$

$$\varphi_{axicon}(x,y) = -2\pi \frac{\sqrt{x^2+y^2}}{d} \tag{2}$$

$$\varphi_{spiral}(x,y) = l \cdot \arctan\left(\frac{x}{y}\right) \tag{3}$$

$$\varphi_{lens}(x,y) = \frac{-\pi(x^2+y^2)}{\lambda f} \tag{4}$$

where x, y represent the position coordinates of the unit cell in the specific column and row in the antenna array with respect to the center of the array. Equation (2) defines an axicon phase profile and d represents the axicon period which controls the ring radius of the PV beam. Equation (3) represents the spiral phase profile of an optical vortex with the parameter l as the TC of PV beam. Equation (4) introduces the phase profile of spherical wave for a Fourier transform lens with the focal length of f, and λ is the operation wavelength.

Such combined unique phase distribution described in Equation (1) integrates the functionalities of axicon, spiral phase plate, and lens at the same time so that the focused PV beam can be directly produced through the metasurface. In our design, the axicon periods d are chosen to be $d = 8$ and 4 μm, and the TC parameters $l = 1, 3, 5,$ and 8 are considered. The focal
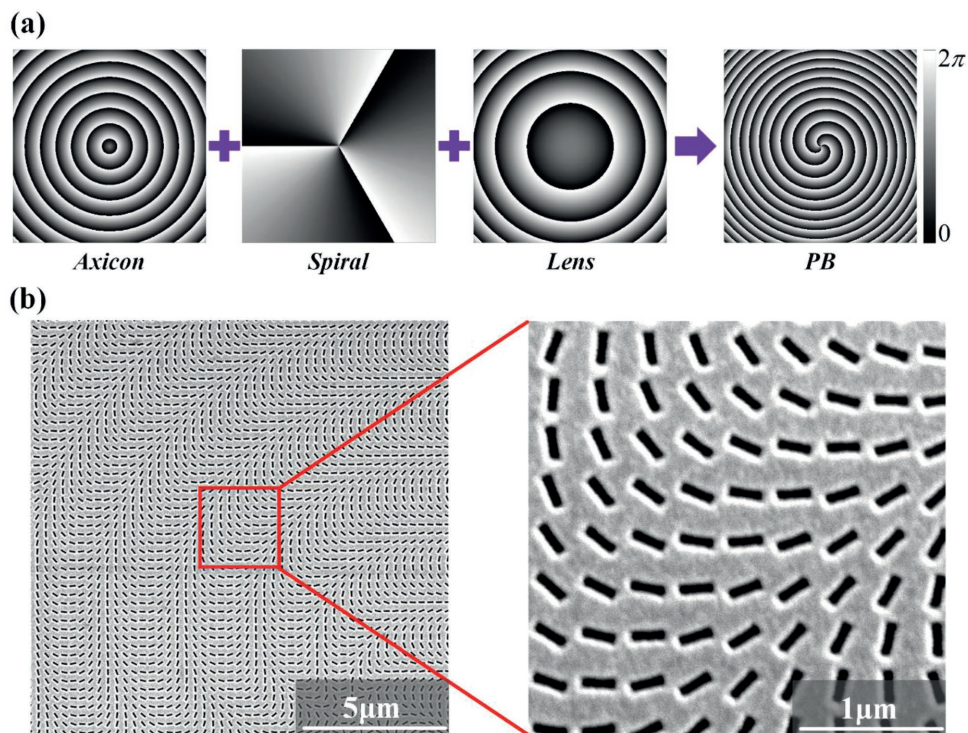

Figure 2. a) Generation steps for the phase profile of PV beam with $d = 4$ μm and $l = 3$. b) SEM images of the fabricated metasurface sample.

**ADVANCED
SCIENCE NEWS**
www.advancedsciencenews.com

**ADVANCED
OPTICAL
MATERIALS**
www.advopticalmat.de

length of the Fourier transform lens is selected as $f = 200$ μm at the wavelength of 633 nm. With the above selected control parameters, there are eight metasurface samples that are fabricated and characterized for the generation of PV beams. Figure 2a displays the designed phase profile with the parameters of $d = 4$ μm and $l = 3$, and the SEM images of the fabricated metasurface sample are shown in Figure 2b. The generation of focused 3D PV beams from the metasurface is then demonstrated. **Figure 3a** plots the schematic of experimental setup. The collimated optical beam from a laser diode at the wavelength of 633, 808, or 988 nm is first transmitted through a linear polarizer and a quarter-wave plate to create a circularly polarized beam. Then a pinhole with diameter of 500 μm is imaged upon the metasurface by a 10× objective lens with the pinhole imaging spot size of 100 μm, which completely illuminates the metasurface area of 50 μm × 50 μm. According to the imaging theory, the wavefront of imaging spot is the same as the wavefront at the pinhole position,

which is nearly a plane wave. In order to observe the generated 3D PV beams, a microscope imaging system including a 20× objective lens, a 0.5× tube lens, and charge-coupled device (CCD) camera is placed on a translation stage behind the metasurface for recording the 3D beam structure. Another set of a quarter-wave plate and a linear polarizer is used to select the converted spin.

The upper row in Figure 3b is the simulated optical intensity distribution of 3D PV beam with parameters of $d = 4$ μm and $l = 3$ at 633 nm, by using the beam diffraction integration method. The bottom row plots the measured cross-section images of 3D PV beam. It is shown in both simulated and experimental results that the circular intensity ring with side lobes starts to evolve from a BG beam after the metasurface and finally perfect annular intensity rings are formed at the positions of $z > 150$ μm. As the PV beam further propagates in the free space, the annular ring shape is maintained invariant but the ring radius gets larger. In Figure 3b, the measured ring
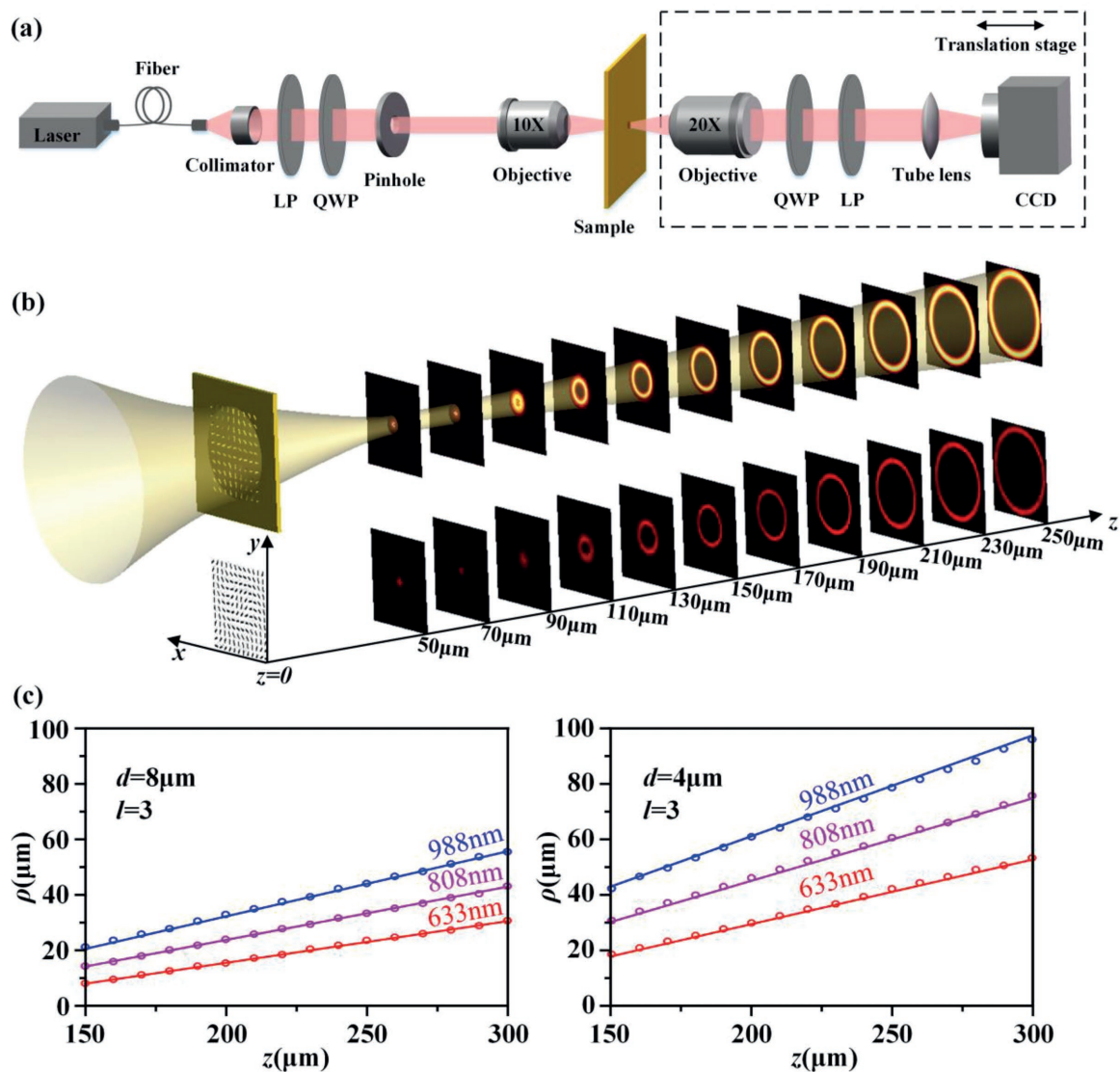

Figure 3. a) Schematic of the experimental setup. b) Simulated and measured optical intensity distributions for the focused 3D PV beams. c) Measured ring radius of PV beam versus the propagation distance z (circular points), and the fitted lines for measured data (solid lines).

**ADVANCED
SCIENCE NEWS**

www.advancedsciencenews.com

**ADVANCED
OPTICAL
MATERIALS**

www.advopticalmat.de

radius ρ of PV beam as a function of the propagation distance at different wavelengths of 633, 808, and 988 nm is plotted for metasurfaces with $l = 3$, $d = 8$ and 4 µm, respectively. For the PV beams generated by the conventional free-space approach with a separate Fourier transform convex lens, the annular ring radius at the image focal plane can be approximated as $\rho = \lambda f/d$.[17] For the current focused 3D PV beams through metasurface samples as shown in Figure 3b, the relationship between the annular ring radius ρ and propagation distance z is almost linear and the fitting function can be expressed as
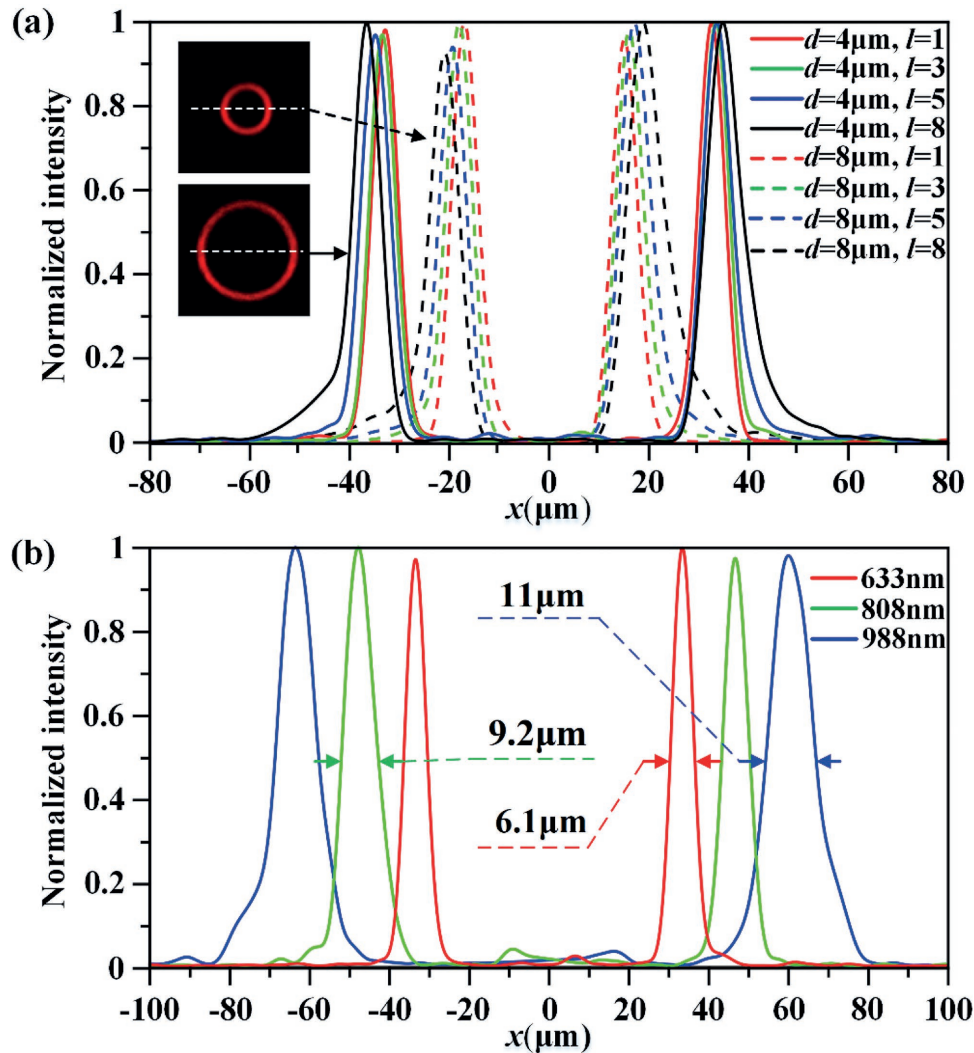
$$\rho(z) = \frac{2.7\lambda}{d+3.4}(z-f) + 400\frac{\lambda-0.3}{d-0.5} \qquad (5)$$

where the lens focal length is $f = 200$ µm and several constants in the unit of micrometer are introduced for the optimized fitting. The fitted lines are also plotted in Figure 3c. It can be seen that the slope and ρ-intercept of the fitted line are determined by both the wavelength λ and axicon period d. The annular ring radius ρ will also be changed linearly by varying the lens focal length f. With such approximated linear fitting function, the ring radius of 3D PV beam located at different propagation distance and at different wavelength can be predicted, which is useful in designing the propagation of multiple 3D PV beams.

In order to further demonstrate the broadband generation of PV beams with the metasurface, **Figure 4** displays the measured intensity distributions of PV beams at propagation
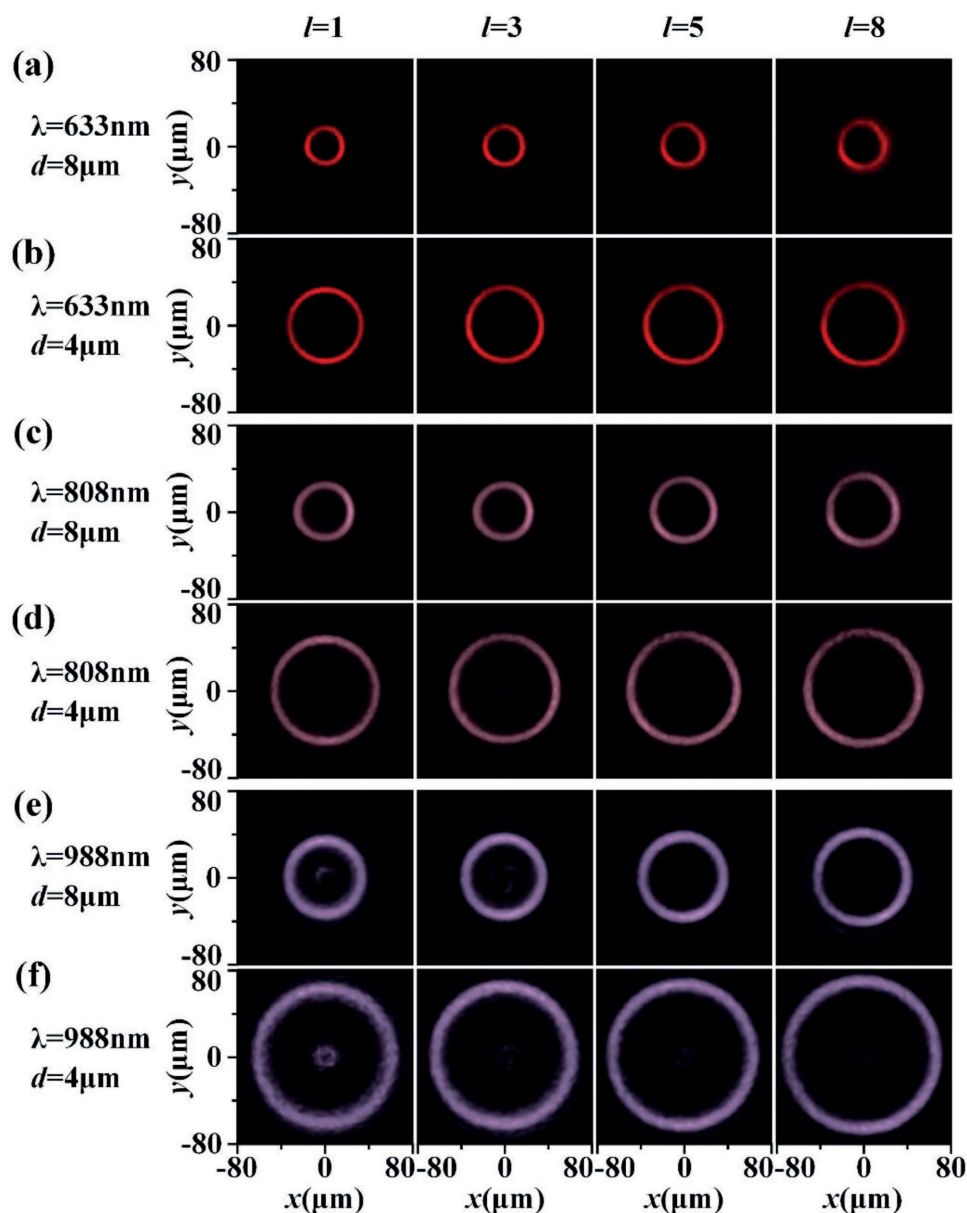
Figure 4. Measured intensity distributions of PV beams at propagation distance of $z = 200$ µm at three wavelengths of 633, 808, and 988 nm. From left column to right column, the topological change l is 1, 3, 5, 8. a,b) The intensity profiles at 633 nm for axicon period $d = 8$ and 4 µm, respectively. c,d) The intensity profiles at 808 nm. e,f) The intensity profiles at 988 nm.
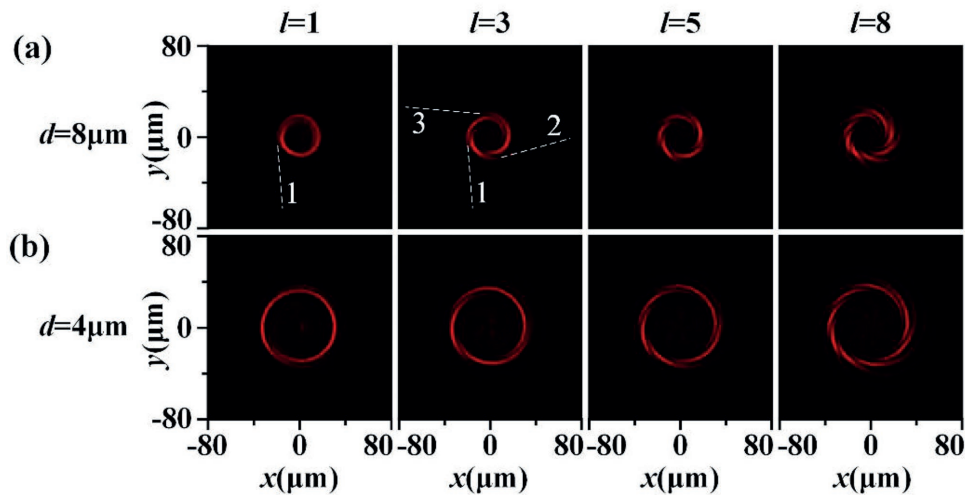
ADVANCED
SCIENCE NEWS

www.advancedsciencenews.com

ADVANCED
OPTICAL
MATERIALS

www.advopticalmat.de

Figure 5. a) Measured cross sections of annular intensity rings at 633 nm at propagation distance $z = 200$ μm with axicon period $d = 8$ μm (dashed line) and 4 μm (solid line). b) Measured cross sections of annular intensity rings for $d = 4$ μm and $l = 3$ at the wavelength of 633 nm (red line), 808 nm (green line), and 988 nm (blue line).

distance of $z = 200$ μm at three wavelengths of 633, 808, and 988 nm for the eight fabricated metasurface samples with different control parameters of TC l and axicon period d. It is observed that at a certain wavelength, the annular ring radius of PV beam is almost unchanged for different TCs under a fixed axicon period. Also the ring radius is nearly doubled when d is reduced from 8 to 4 μm. The ring radius is also enlarged as the wavelength is increased, as predicated in Figure 3b. The observed annular intensity rings of PV beams have good quality at all different wavelengths, indicating the broadband operation capabilities of the metasurface. Next, the measured cross sections of the annular intensity rings in different TCs and at different wavelengths are compared to investigate the properties of ring width and ring diameter. **Figure 5**a shows the cross sections of annular intensity rings at 633 nm at propagation distance of $z = 200$ μm, giving the relationship between ring width and TC. It is observed that the ring radius of PV beam is nearly the same but the ring width tends to broaden as

TC is increased. Figure 5b gives the cross sections of annular intensity rings at three wavelengths for $d = 4$ μm and $l = 3$. It is shown that for the same metasurface sample, as the wavelength is increased, the generated ring radius of PV beam will get larger and the ring width will also tend to broaden. **Figure 6** presents the captured interferometry patterns at $z = 200$ μm where the PV beams interfere with the reference spherical wave at 633 nm. It is clearly seen that the continuous annular intensity ring structure breaks into several spiral branches in the interferometry patterns. The TCs of PV beams can be identified by examining the number of spiral branches of the interferometry patterns, as shown in Figure 6.

Recently, polarization-controllable multichannel superpositions of OAM states with various TCs have been realized by using a single PBOE-based metasurface.[44] In our case, the single metasurface is designed to generate multiple 3D PV beams. The 3D PV beam arrays support controllable vortex positions and multiple TCs, which are useful in OAM-multiplexing

ADVANCED
SCIENCE NEWS

www.advancedsciencenews.com

ADVANCED
OPTICAL
MATERIALS

www.advopticalmat.de

Figure 6. The captured interferometry patterns at $z = 200\,\mu m$ at 633 nm. From left column to right column, the TC is 1, 3, 5, and 8. a) The axicon period is $d = 8\,\mu m$. b) $d = 4\,\mu m$.

communications. The phase profile for generating the PV beam array are determined by superimposing the complex amplitudes of different single PV beams and then calculating the argument of the summation complex function.[17–19,44] The PB phase profile for one single PV beam is shown in Equation (1). By introducing linear phase gradients along both x and y directions with complex functions of $\exp(i2\pi x/\Lambda_x)$ and $\exp(i2\pi y/\Lambda_y)$, where Λ_x and Λ_y are the phase fringe periods, the PV beam will propagate along a certain diffraction angle off the z direction. Each PV beam is designed to diffract along a specific angle in space so that the overall phase profile for assembling the multiple PV beams together can be expressed as

$$\varphi_{sum}(x,y) = \arg\left\{\sum_{n=1}^{4}\exp\left[i\left(\varphi_{PB,n} + a_n\frac{2\pi x}{\Lambda_x} + b_n\frac{2\pi y}{\Lambda_y}\right)\right]\right\} \quad (6)$$

where a_n and b_n are parameters with values of 0 or ± 1 to control the linear phase gradients along the x direction and the y direction, respectively. In the design, the ring radius at propagation distance z should be less than the spacing between two adjacent PV annular intensity rings, which can be satisfied by considering the PV beam shifts along x and y directions at propagation distance z

$$S_x = a_n \cdot \frac{\lambda z}{\Lambda_x} \quad (7)$$

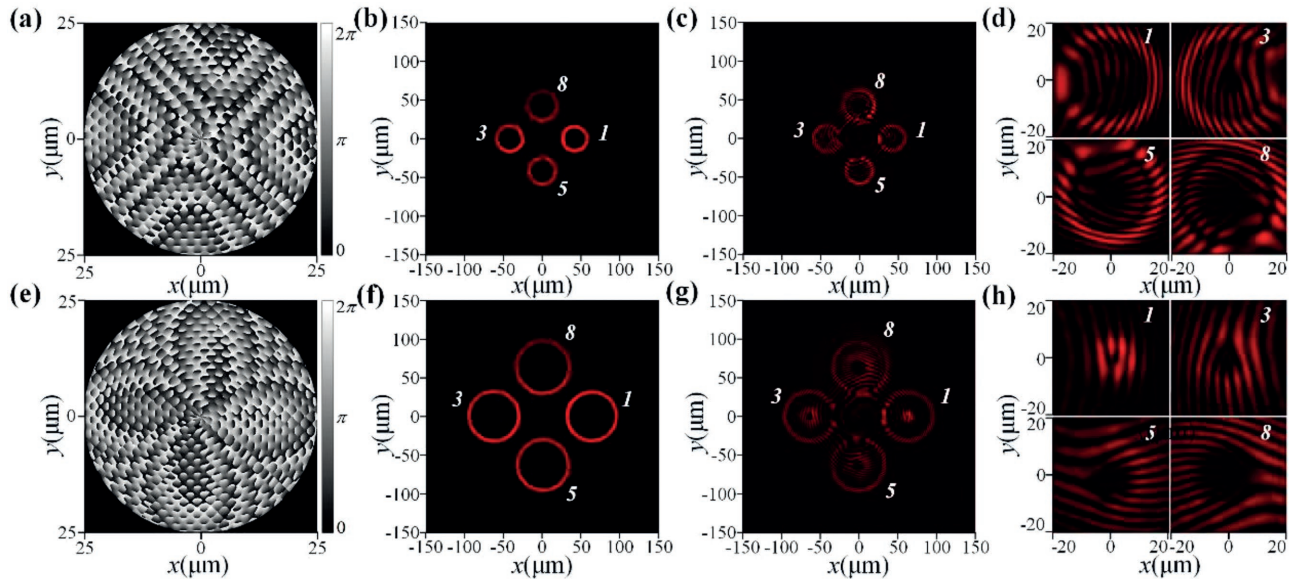$$S_y = b_n \cdot \frac{\lambda z}{\Lambda_y} \quad (8)$$

Here, two multiple PV beam arrays are demonstrated at 633 nm and each of them consists four single PV beams, as shown in **Figure 7**. For the first PV beam array in small ring radius with the same axicon period $d = 8\,\mu m$, lens focal length $f = 200\,\mu m$, and $\Lambda_x = \Lambda_x = 3\,\mu m$ shown in Figure 7a–d, the parameters for each single PV beam are listed as follows,

PV$_1$ ($l = 1$, $a_n = 1$, $b_n = 0$), PV$_2$ ($l = 3$, $a_n = -1$, $b_n = 0$), PV$_3$ ($l = 5$, $a_n = 0$, $b_n = 1$), and PV$_4$ ($l = 8$, $a_n = 0$, $b_n = -1$). The PB phase profile to produce this PV beam array is shown in Figure 7a, and the intensity distribution of the PV beam array at propagation distance $z = 200\,\mu m$ is shown in Figure 7b. It is shown that the four annular intensity rings with different TCs have the same ring radius. And the center positions of four PV beams are located at (42.2 µm, 0), (−42.2 µm, 0), (0, 42.2 µm), and (0, −42.2 µm), respectively, which agree with the beam position shifts (S_x, S_y) calculated from Equations (7) and (8). For the second PV beam array in large ring radius with $d = 4\,\mu m$, $f = 200\,\mu m$, and $\Lambda_x = \Lambda_x = 2\,\mu m$ shown in Figure 7e–h, the parameters for each single PV beam are listed as follows, PV$_1$ ($l = 1$, $a_n = 1$, $b_n = 0$), PV$_2$ ($l = 3$, $a_n = -1$, $b_n = 0$), PV$_3$ ($l = 5$, $a_n = 0$, $b_n = 1$), and PV$_4$ ($l = 8$, $a_n = 1$, $b_n = -1$). To avoid the spatial overlap between the neighboring PV beams, the center positions of four PV beams are set as (63.3 µm, 0), (−63.3 µm, 0), (0, 63.3 µm), and (0, −63.3 µm), respectively. The corresponding PB phase profile and the intensity distribution of the PV beam array at $z = 200\,\mu m$ are displayed in Figure 7e,f. In this case, the four annular intensity rings have the same ring radius with large size. Furthermore, the interferometry patterns are recorded at $z = 200\,\mu m$ where each PV beam array interferes with the reference plane wave at 633 nm. Figure 7c,g shows original interferometry patterns while Figure 7d,h shows the magnified patterns. The interfered fork-shaped fringe patterns can be observed near the PV beam centers, and the characteristic fork fringe number reflects the TC of each PV beam as 1, 3, 5, and 8, which is coincident with the beam array design.

3. Conclusion

In summary, we have proposed and demonstrated plasmonic metasurfaces consisting of rectangular-hole antennas as integrated beam converters to directly generate the focused 3D PV beams and multiple PV beam arrays in a broad wavelength range. The designed metasurface produces a unique

ADVANCED
SCIENCE NEWS
www.advancedsciencenews.com

ADVANCED
OPTICAL
MATERIALS
www.advopticalmat.de

Figure 7. a,e) The phase profiles to generate four PV beam arrays for $d = 8$ and 4 µm, respectively. b,f) The intensity distributions of the generated PV beam arrays at propagation distance $z = 200$ µm. c,g) The recorded interferometry patterns of the PV beam arrays. d,h) The magnified interferometry patterns with fork-shaped fringes.

complex phase profile containing the superimposed phase distributions of axicon, spiral phase plate, and Fourier transform lens at the same time for the direct PV beam generation. This new type of compact PV beam generator will find many potential applications in OAM- and wavelength-multiplexed fiber communication, optical particle trapping and transport, quantum optics and laser manufacturing, as well as create new opportunities in building novel metasurface-based devices for structured light manipulation and beam conversion.

4. Experimental Section

Numerical Simulations: The simulations shown in Figure 1 are conducted by using the finite integration time domain solver of the computer simulation technology (CST) Microwave Studio software. In the simulation, periodic boundary conditions are employed along both x and y directions in the rectangular-hole unit cell. The permittivity of gold is taken from spectroscopic ellipsometry data fitted with a general oscillator model, and the refractive index of glass substrate is 1.45. The beam propagation in free space of the focused 3D PV beam shown in Figure 3a is calculated by using the Fresnel–Kirchhoff diffraction integral

$$U(x,y,z) = \frac{1}{i\lambda} \iint_S U(x_0,y_0) \left[\frac{\cos(\bar{n},r) - \cos(\bar{n},r')}{2} \right] \frac{e^{ikr}}{r} dS \quad (9)$$

where $U(x_0,y_0)$ is the complex amplitude distribution of PV beam located at the $z = 0$ plane with surface area S and normal direction $\bar{n}$, r' is the vector between the source point and a point in the $z = 0$ plane, $\mathbf{r}$ is the vector between the point in $z = 0$ plane, and a point in the plane at the propagation distance z ranging from 50 to 500 µm, and $k = 2\pi/\lambda$ is the wavevector.

Sample Fabrication: A 50 nm thick gold film is deposited on a glass substrate using electron-beam evaporation. Then the designed rectangular-hole arrays are milled in the gold film using focused ion beam (FIB) system (FEI Helios Nanolab 600, 30 kV, 9.7 pA). Each

metasurface sample contains 150 × 150 unit cells, and each unit cell contains a milled subwavelength rectangular hole with size of 200 nm × 60 nm at a specified orientation angle. According to the designed PB phase profiles, the orientation angle for the rectangular-hole antenna in each unit cell is determined and used in the FIB fabrication of metasurface sample.

Optical Characterization: The transmission spectra through the metasurface sample under linear polarization basis and circular polarization basis shown in Figure 1 are measured with a collimated broadband tungsten–halogen source, where a combination of a linear polarizer and an achromatic quarter-wave plate are used to convert the incident light to circularly polarized wave. The light beam is focused normally onto the sample using a 50× objective lens and the transmitted light is collected by another 10× objective lens to a spectrometer (Horiba, iHR 550). Another set of a quarter-wave plate and a linear polarizer is used to distinguish the original and converted circular polarization state transmitted through the metasurface. A transparent glass substrate is utilized to normalize the transmission spectra. Since the metasurface sample operates in a broad wavelength range from 600 to 1000 nm, three diode lasers operating at different wavelengths of 633, 808, and 988 nm are employed in the PV beam experiments. The 3D beam structures of the generated PV beams are captured by a microscope imaging system with a 20× objective lens, a 0.5× tube lens, and CCD camera placed on a translation stage, as shown in Figure 3a.

Conflict of Interest

The authors declare no conflict of interest.

Keywords

[1] L. Allen, M. W. Beijersbergen, R. Spreeuw, J. Woerdman, *Phys. Rev. A* **1992**, *45*, 8185.

[2] R. Fickler, R. Lapkiewicz, W. N. Plick, M. Krenn, C. Schaeff, S. Ramelow, A. Zeilinger, *Science* **2012**, *338*, 640.

[3] B. C. Hiesmayr, M. J. A. De Dood, W. Löffler, *Phys. Rev. Lett.* **2016**, *116*, 073601.

[4] D. Grier, *Nature* **2003**, *424*, 810.

[5] S. Albaladejo, M. I. Marqués, M. Laroche, J. J. Sáenz, *Phys. Rev. Lett.* **2009**, *102*, 113602.

[6] J. Wang, J. Yang, I. M. Fazal, N. Ahmed, Y. Yan, H. Huang, Y. Ren, Y. Yue, S. Dolinar, M. Tur, A. E. Willner, *Nat. Photonics* **2012**, *6*, 488.

[7] D. Richardson, J. Fini, L. Nelson, *Nat. Photonics* **2013**, *7*, 354.

[8] H. Yan, E. Zhang, B. Zhao, K. Duan, *Opt. Express* **2012**, *20*, 17904.

[9] S. Li, J. Wang, *IEEE Photonics J.* **2013**, *5*, 7101007.

[10] S. Ramachandran, P. Gregg, P. Kristensen, S. E. Golowich, *Opt. Express* **2015**, *23*, 3721.

[11] A. S. Ostrovsky, C. Rickenstorff-Parrao, V. Arrizón, *Opt. Lett.* **2013**, *38*, 534.

[12] J. García-García, C. Rickenstorff-Parrao, R. Ramos-García, V. Arrizón, A. S. Ostrovsky, *Opt. Lett.* **2014**, *39*, 5305.

[13] Y. Liu, Y. Ke, J. Zhou, Y. Liu, H. Luo, S. Wen, D. Fan, *Sci. Rep.* **2017**, *7*, 44096.

[14] P. Vaity, L. Rusch, *Opt. Lett.* **2015**, *40*, 597.

[15] A. Vijayakumar, S. Bhattacharya, *Opt. Eng.* **2015**, *54*, 111310.

[16] D. Deng, Y. Li, Y. Han, X. Su, J. Ye, J. Gao, Q. Sun, S. Qu, *Opt. Express* **2016**, *24*, 28270.

[17] S. Fu, T. Wang, C. Gao, *J. Opt. Soc. Am. A* **2016**, *33*, 1836.

[18] J. Yu, C. Zhou, Y. Lu, J. Wu, L. Zhu, W. Jia, *Opt. Lett.* **2015**, *40*, 2513.

[19] S. Yu, L. Li, G. Shi, C. Zhu, Y. Shi, *Appl. Phys. Lett.* **2016**, *108*, 241901.

[20] M. Chen, M. Mazilu, Y. Arita, E. M. Wright, K. Dholakia, *Opt. Lett.* **2013**, *38*, 4919.

[21] C. Zhang, C. Min, L. Du, X. Yuan, *Appl. Phys. Lett.* **2016**, *108*, 201601.

[22] P. Gregg, P. Kristensen, S. Ramachandran, *Optica* **2015**, *2*, 2334.

[23] J. Ye, Y. Li, Y. Han, D. Deng, Z. Guo, J. Gao, Q. Sun, Y. Liu, S. Qu, *Opt. Express* **2016**, *24*, 8310.

[24] M. V. Jabir, N. Apurv Chaitanya, A. Aadhi, G. K. Samanta, *Sci. Rep.* **2016**, *6*, 21877.

[25] Z. Kuang, W. Perrie, S. P. Edwardson, E. Fearon, G. Dearden, *J. Phys. D: Appl. Phys.* **2014**, *47*, 115501.

[26] A. V. Kildishev, A. Boltasseva, V. M. Shalaev, *Science* **2013**, *339*, 1232009.

[27] N. Yu, F. Capasso, *Nat. Mater.* **2014**, *13*, 139.

[28] M. V. Berry, *Proc. R. Soc. London, Ser. A* **1984**, *392*, 45.

[29] M. V. Berry, *J. Mod. Opt.* **1987**, *34*, 1401.

[30] A. Niv, G. Biener, V. Kleiner, E. Hasman, *Opt. Express* **2006**, *14*, 4208.

[31] E. Hasman, V. Kleiner, G. Biener, A. Niv, *Appl. Phys. Lett.* **2003**, *82*, 328.

[32] Z. e. Bomzon, V. Kleiner, E. Hasman, *Opt. Lett.* **2001**, *26*, 1424.

[33] Z. e. Bomzon, G. Biener, V. Kleiner, E. Hasman, *Opt. Lett.* **2002**, *27*, 285.

[34] F. Gori, *Opt. Lett.* **1999**, *24*, 584.

[35] E. Karimi, S. A. Schulz, I. De Leon, H. Qassim, J. Upham, R. W. Boyd, *Light: Sci. Appl.* **2014**, *3*, e167.

[36] L. Huang, X. Chen, H. Muhlenbernd, G. Li, B. Bai, Q. Tan, G. Jin, T. Zentgraf, S. Zhang, *Nano Lett.* **2012**, *12*, 5750.

[37] J. Zeng, L. Li, X. Yang, J. Gao, *Nano Lett.* **2016**, *16*, 3101.

[38] J. Zeng, J. Gao, T. S. Luk, N. M. Litchinitser, X. Yang, *Nano Lett.* **2015**, *15*, 5363.

[39] J. Zeng, T. S. Luk, J. Gao, X. Yang, *Sci. Rep.* **2017**, *7*, 11824.

[40] A. Arbabi, Y. Horie, M. Bagheri, A. Faraon, *Nat. Nanotechnol.* **2015**, *10*, 937.

[41] W. T. Chen, M. Khorasaninejad, A. Y. Zhu, J. Oh, R. C. Devlin, A. Zaidi, F. Capasso, *Light: Sci. Appl.* **2017**, *6*, e16259.

[42] L. Zhang, S. Liu, L. Li, T. J. Cui, *ACS Appl. Mater. Interfaces* **2017**, *9*, 36447.

[43] Q. Ma, C. B. Shi, G. D. Bai, T. Y. Chen, A. Noor, T. J. Cui, *Adv. Opt. Mater.* **2017**, *5*, 1700548.

[44] F. Yue, D. Wen, C. Zhang, B. D. Gerardot, W. Wang, S. Zhang, X. Chen, *Adv. Mater.* **2017**, *29*, 1603838.

[45] E. Maguid, I. Yulevich, D. Veksler, V. Kleiner, M. L. Brongersma, E. Hasman, *Science* **2016**, *352*, 1202.

[46] F. Aieta, P. Genevet, M. A. Kats, N. Yu, R. Blanchard, Z. Gaburro, F. Capasso, *Nano Lett.* **2012**, *12*, 4932.

[47] X. Ni, S. Ishii, A. V. Kildishev, V. M. Shalaev, *Light: Sci. Appl.* **2013**, *2*, e72.

[48] X. Chen, L. Huang, H. Muhlenbernd, G. Li, B. Bai, Q. Tan, G. Jin, C. Qiu, S. Zhang, T. Zentgraf, *Nat. Commun.* **2012**, *3*, 1198.

[49] M. Khorasaninejad, W. T. Chen, A. Y. Zhu, J. Oh, R. C. Devlin, D. Rousso, F. Capasso, *Nano Lett.* **2016**, *16*, 4595.

[50] N. Yu, F. Aieta, P. Genevet, M. A. Kats, Z. Gaburro, F. Capasso, *Nano Lett.* **2012**, *12*, 6328.

[51] Y. Zhao, A. Alu, *Nano Lett.* **2013**, *13*, 1086.

[52] W. Cao, X. Yang, J. Gao, *Sci. Rep.* **2017**, *7*, 8841.

[53] W. Wan, J. Gao, X. Yang, *Adv. Opt. Mater.* **2017**, *5*, 1700541.

[54] W. Wan, J. Gao, X. Yang, *ACS Nano* **2016**, *10*, 10671.

[55] X. Ni, A. V. Kildishev, V. M. Shalaev, *Nat. Commun.* **2013**, *4*, 2807.

[56] L. Huang, X. Chen, H. Muhlenbernd, H. Zhang, S. Chen, B. Bai, Q. Tan, G. Jin, K. Cheah, C. Qiu, J. Li, T. Zentgraf, S. Zhang, *Nat. Commun.* **2013**, *4*, 2808.

[57] G. Zheng, H. Muhlenbernd, M. Kenney, G. Li, T. Zentgraf, S. Zhang, *Nat. Nanotechnol.* **2015**, *10*, 308.